lubricants

MDPI

Article

Transformation from $D0_{22}$ to $L1_2$ in Al_3Ti by Fe Addition for Enhanced Wear Resistance

Guijiang Diao [1], Junfeng Yuan [2], Anqiang He [1], Dong Zhang [1], Aakash Kumar [1], Ranran Fang [3], Anatoliy Vorobyev [3], Wengang Chen [4] and Dongyang Li [1,*]

[1] Department of Chemical and Materials Engineering, University of Alberta, Edmonton, AB T6G 2H5, Canada; guijiang@ualberta.ca (G.D.); ahe@ualberta.ca (A.H.); dzhang5@ualberta.ca (D.Z.); aakash1@ualberta.ca (A.K.)
[2] School of Mechatronic Engineering, China University of Mining and Technology, Xuzhou 221116, China; yuanjf@cumt.edu.cn
[3] School of Optoelectronic Engineering, Chongqing University of Posts and Telecommunications, Chongwen Road, Nanan District, Chongqing 400065, China; fangrr@cqupt.edu.cn (R.F.); ayv@cqupt.edu.cn (A.V.)
[4] School of Machinery and Transportation, Southwest Forestry University, Kunming 650224, China; chenwengang999@163.com
* Correspondence: dongyang.li@ualberta.ca

Abstract: The addition of third elements may help transform brittle $D0_{22}$-structured lightweight Al_3Ti to a relatively ductile $L1_2$-structured $(Al, M)_3Ti$ (where M represents the third elements), thus increasing the ductility at the expense of hardness. Such a transformation could benefit the wear resistance of the alloy due to improved toughness if a proper balance between the hardness and ductility is achieved. In this work, a $D0_{22}$-predominant Al_3Ti alloy (S-Al_3Ti) and an $L1_2$-predominant $(Al, Fe)_3Ti$ alloy (S-$Al_{67}Ti_{25}Fe_8$) were fabricated by arc melting. Change in wear resistance, corresponding to a $D0_{22}$-to-$L1_2$ transformation, caused by the addition of Fe as a representative third element, was investigated and compared with the wear resistance of a commercial Al-matrix composite reinforced by 30 wt.% SiC particles (S-Al/SiC_p) as a reference material. It was observed that wear of the S-Al_3Ti resulted from abrasion involving synergistic oxidation, leading to a larger volume loss. In contrast, the softer S-$Al_{67}Ti_{25}Fe_8$ showed enhanced wear resistance, benefiting from improved toughness with reasonable hardness. During the wear testing, both the alloys exhibited better performance than S-Al/SiC_p, a well-known lightweight composite. This study highlights that $D0_{22}$-to-$L1_2$ transformation enhances wear resistance due to increased toughness which can be adjusted using the addition of a third element.

Keywords: $D0_{22}$ Al_3Ti; $L1_2$ $(Al, Fe)_3Ti$; phase transformation; wear resistance

check for updates

Citation: Diao, G.; Yuan, J.; He, A.; Zhang, D.; Kumar, A.; Fang, R.; Vorobyev, A.; Chen, W.; Li, D. Transformation from $D0_{22}$ to $L1_2$ in Al_3Ti by Fe Addition for Enhanced Wear Resistance. *Lubricants* **2024**, *12*, 398. https://doi.org/10.3390/lubricants12110398

Received: 12 October 2024
Revised: 13 November 2024
Accepted: 15 November 2024
Published: 19 November 2024

Copyright: © 2024 by the authors. Licensee MDPI, Basel, Switzerland. This article is an open access article distributed under the terms and conditions of the Creative Commons Attribution (CC BY) license (https://creativecommons.org/licenses/by/4.0/).

1. Introduction

Al-Ti intermetallic compounds are very attractive candidates for the structural components used at elevated temperatures due to their low density, high melting point and high specific strength [1–3]. The long-range ordering in the intermetallic compounds effectively impedes atomic diffusion and pin dislocations, leading to a high resistance to softening at elevated temperatures, compared to solid-solution alloys [4,5]. According to the Al-Ti binary phase diagram, four Al-Ti intermetallic compounds, i.e., AlTi, Al_2Ti, Al_3Ti and Ti_3Al, are promising for high-temperature applications [6], and Al_3Ti is the most appealing due to its advantageous density [7].

Binary Al_3Ti may have two commonly encountered crystal structures; one is a stable tetragonal $D0_{22}$ structure with a certain degree of anisotropy due to its low symmetry, and the other is a metastable cubic $L1_2$ structure with relatively isotropic properties due to its higher symmetry [8]. Figure 1 illustrates the crystal structures of $D0_{22}$ Al_3Ti and $L1_2$ Al_3Ti. Yamaguchi et al. [9] reported that the primary deformation mode of $D0_{22}$ Al_3Ti during compression below 620 °C is <111> [112] twinning, with a dislocation slip activated at

higher temperatures, resulting in improved ductility. The brittleness of the $D0_{22}$ structure at room temperature, because of its insufficient slip systems [10], remains a significant challenge for practical applications of Al_3Ti [11].

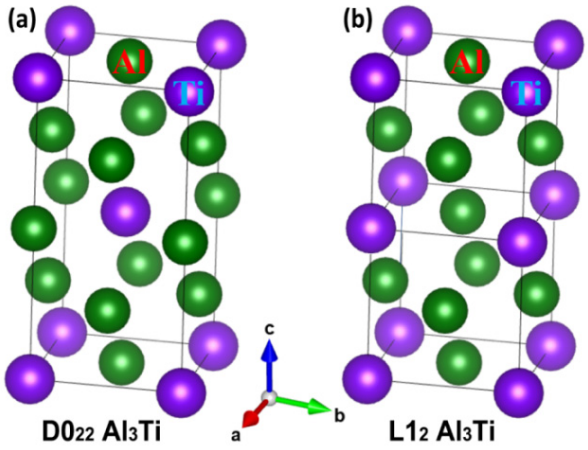


Figure 1. Schematic illustrations of crystal structures of (**a**) $D0_{22}$ Al_3Ti and (**b**) $L1_2$ Al_3Ti.

The $D0_{22}$ structure is more ionic with stronger bonding than that of $L1_2$ structure. In the $D0_{22}$ structure, Ti atoms gain charges and Al atoms lose charges [12]. Alloying Al_3Ti with a small amount of one or multiple transition metal elements, such as Cr, Mn, Fe, Ni, Cu, and Ag [13–21], can transform the tetragonal $D0_{22}$ structure into the cubic $L1_2$ structure. These less electropositive third elements may replace Al, taking electrons from Al and suppressing the charge transfer from Al to Ti, which stabilizes the $L1_2$ structure [22,23]. The cubic $L1_2$ structure provides more slip systems for plastic deformation, thus enhancing the ductility. The $D0_{22}$-to-L_{12} transformation can help achieve improved plasticity, which is beneficial to practical applications of Al_3Ti. In general, the improvement in plasticity is achieved at the expense of strength and hardness, which may lead to negative influence on some properties such as the resistance to wear [24]. A theoretical study on tetragonal-$D0_{22}$ and cubic-$L1_2$ structures via calculations with density functional theory by Boulechfar et al. [25] demonstrated that the $L1_2$ phase showed lowered brittleness and hardness as well, compared to the $D0_{22}$ structure. Milman et al. [26] compared the hardness of tetragonal Al_3Ti with that of cubic $L1_2$ Cr-doped $Al_{61}Cr_{12}Ti_{27}$ and Mn-doped $Al_{66}Mn_{11}Ti_{23}$, and observed that the hardness decreased by about 40% with Cr doping and 60% with Mn doping, respectively.

Wear, as one of the material failure processes, occurs when two surfaces rub each other, causing surface damage or failure. Estimates show that up to 80% of machine parts failure involves wear [27]. The economic loss caused by friction and wear reaches 2~7% of the gross domestic product for industrial countries [27]. Wear is a complex failure process, influenced by many factors, e.g., environmental aggressiveness, the wear loading condition, and microstructure modification, etc. [28–32], which could be mitigated using different approaches, including alloying, microstructure engineering, heat treatment, and texture engineering, etc. [33–37]. Mechanical properties, such as properly balanced hardness/strength and ductility/toughness, are indispensable to desirable wear resistance. Given the improved ductility and reduced strength/hardness by the transformation from the hard but brittle $D0_{22}$ Al_3Ti to the ductile $L1_2$ $(Al, M)_3Ti$ (where M represents ternary elements), the corresponding wear resistance is accordingly affected, which should be adjustable by tuning the balance between hardness and ductility or toughness. However, there are few studies on the wear behaviors of $D0_{22}$ Al_3Ti and $L1_2$ $(Al, M)_3Ti$ reported in the literature. It is, thus, of importance to investigate how the wear resistance is affected by the phase transformation.

The objectives of this study are (1) to investigate the wear behavior of tetragonal $D0_{22}$ Al_3Ti and that of cubic $L1_2$ $(Al, M)_3Ti$ with improved ductility but reduced hardness, and

(2) to reveal the underlying mechanism for corresponding variations in microstructure and relevant properties in order to further improve or optimize the alloy system. For details, the following tasks were undertaken in this study:

(a) Fe was selected as a representative third element to be alloyed into Al_3Ti, turning the $D0_{22}$-structured Al_3Ti to a ductile $L1_2$ structure $(Al, M)_3Ti$. Fe was selected for this study based on the consideration of its abundant resource, low cost, and the industrial relevance or interest in ferrous alloys. It should be indicated that adding Fe would not affect the alloy's resistance to corrosion, since the alloy contains passive elements Al and Ti of high concentrations, which generate a protective passive film that can prevent continuous corrosion when used in corrosive environments;

(b) The wear resistances of the two fabricated alloys were evaluated, in comparison to that of a well-known 30 wt.% SiC particle-reinforced Al-matrix composite as a reference material;

(c) Corresponding changes in the microstructure, mechanical properties, and wear behavior were analyzed in detail in order to elucidate the underlying wear mechanisms for further improvement or optimization.

2. Materials and Methods

Two alloys, with nominal compositions of Al_3Ti and $Al_{67}Ti_{25}Fe_8$ (in molar ratio or at.%, denoted as S-Al_3Ti and S-$Al_{67}Ti_{25}Fe_8$, respectively), were fabricated using an arc melting process. High-purity Al, Ti and Fe powders ($\geq$99.9%) were mixed and pressed into disk-like bulks, followed by arc melting in a water-cooled copper hearth using an arc melting furnace (MRF Inc., Allenstown, NH, USA) in a protective argon atmosphere. The sample preparation procedures are pictorially illustrated in Figure 2. Both of the samples were re-melted four times to minimize the chemical inhomogeneity.

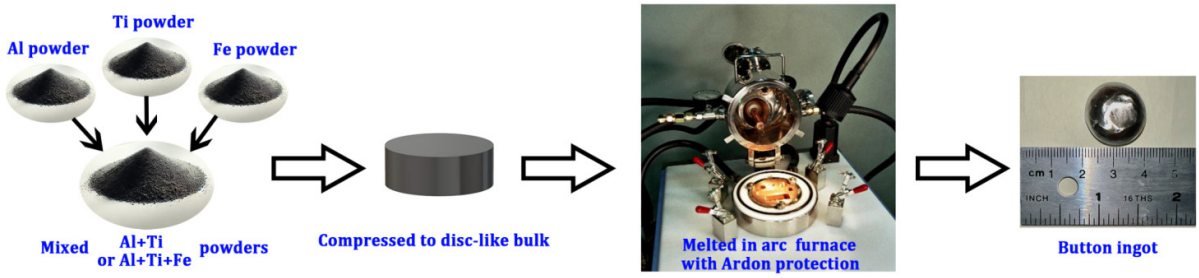


Figure 2. The preparation procedures of S-Al_3Ti and S-$Al_{67}Ti_{25}Fe_8$.

The crystal structure and phases of the alloys were analyzed using an X-ray diffractometer (Rigaku XRD Ultima IV, Tokyo, Japan) at a scanning speed of 4°/min. The microstructure was characterized using a scanning electron microscope (Zeiss EVO M10 SEM, Carl Zeiss AG, Oberkochen, Germany) equipped with energy-dispersive X-ray spectroscopy (EDS) after mechanically grinding and polishing.

The macro-hardness of the alloys was measured using a ZHR Rockwell hardness tester (ZwickRoell, Kennesaw, GA, USA) with a conical diamond indenter under a load of 60 kgf at room temperature. Each polished sample was tested by indentation in 5 randomly selected positions to obtain the average hardness, and error bars were then determined based on the standard deviation. The indentation marks made by a diamond indenter with a square pyramid shape under a load of 15 kgf were observed to visually compare the toughness of the samples.

Sliding wear tests were performed using a ball-on-disk tribometer (CSEM Instruments, Peseux, Switzerland). A silicon nitride (Si_3N_4) ball with a diameter of 3 mm was used as the counter-face to wear the alloy samples at room temperature. The samples were ground and polished before the wear tests. The duration of each test was 30 min. The applied normal load was 3 N. The rotary speed was 191 rpm with a circular path of about 2 mm in

diameter. The wear test for each sample was repeated three times to obtain the average value of wear volume loss. The volume losses from the wear tracks and the worn surface morphologies of the samples were automatically measured and analyzed, respectively, using a three-dimensional (3D) optical profilometer (ZeGage™ Pro, Zygo, Middlefield, CT, USA) with installed software (version 1.14.38, ZeMaps). The worn surfaces were further characterized using SEM with EDS.

3. Results

3.1. Microstructure Characterization

The XRD pattern of S-Al_3Ti is displayed in Figure 3a. The main peaks of the $D0_{22}$ Al_3Ti phase are accompanied by several small peaks of a second phase which is identified as pure Al, indicating that the $D0_{22}$ Al_3Ti phase is predominant in the S-Al_3Ti alloy. The microstructure of S-Al_3Ti was examined by SEM in the back-scattered electron (BSE) mode, and is illustrated in Figure 3b,c. One may see that the second phase is distributed along grain boundaries, which accounts for approximately 3 vol.%. The EDS results shown in Figure 3d–f confirm the presence of Al as second phase, along with the predominant $D0_{22}$ Al_3Ti phase.

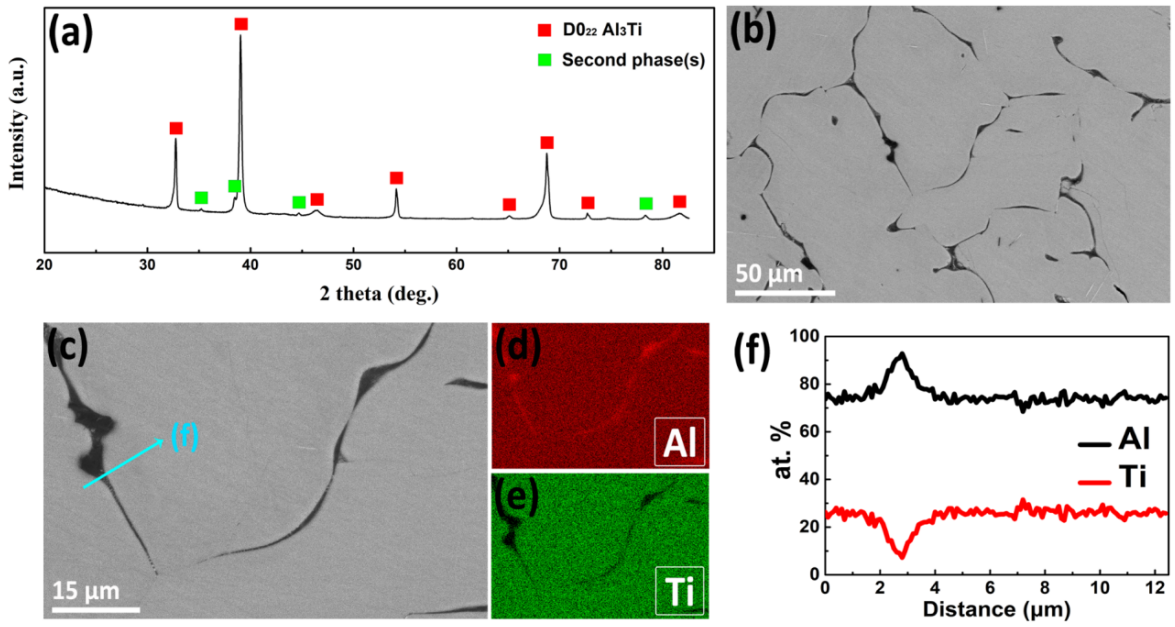


Figure 3. Microstructure characterization for S-Al_3Ti. (**a**) XRD pattern; (**b**,**c**) SEM-BSE images; (**d**,**e**) elemental distributions of the same area in (**c**); (**f**) elemental distribution along the blue line in (**c**).

The XRD pattern of S-$Al_{67}Ti_{25}Fe_8$ is shown in Figure 4a. The main peaks come from the $L1_2$ phase, accompanied by several small peaks of second phase(s), indicating that S-$Al_{67}Ti_{25}Fe_8$ was dominated by the $L1_2$ phase. The microstructure of S-$Al_{67}Ti_{25}Fe_8$ observed with the SEM in BSE mode is shown in Figure 4b,c. One may see that there are two second phases: one is a light gray phase and the other is a bright one inside the light gray phase, which account for approximately 7 vol.% in total. The EDS results presented in Figure 4d–g confirm that the $L1_2$ predominant phase has a composition of $(Al, Fe)_3Ti$, and show that the second phases are Fe-rich with depleted Ti.

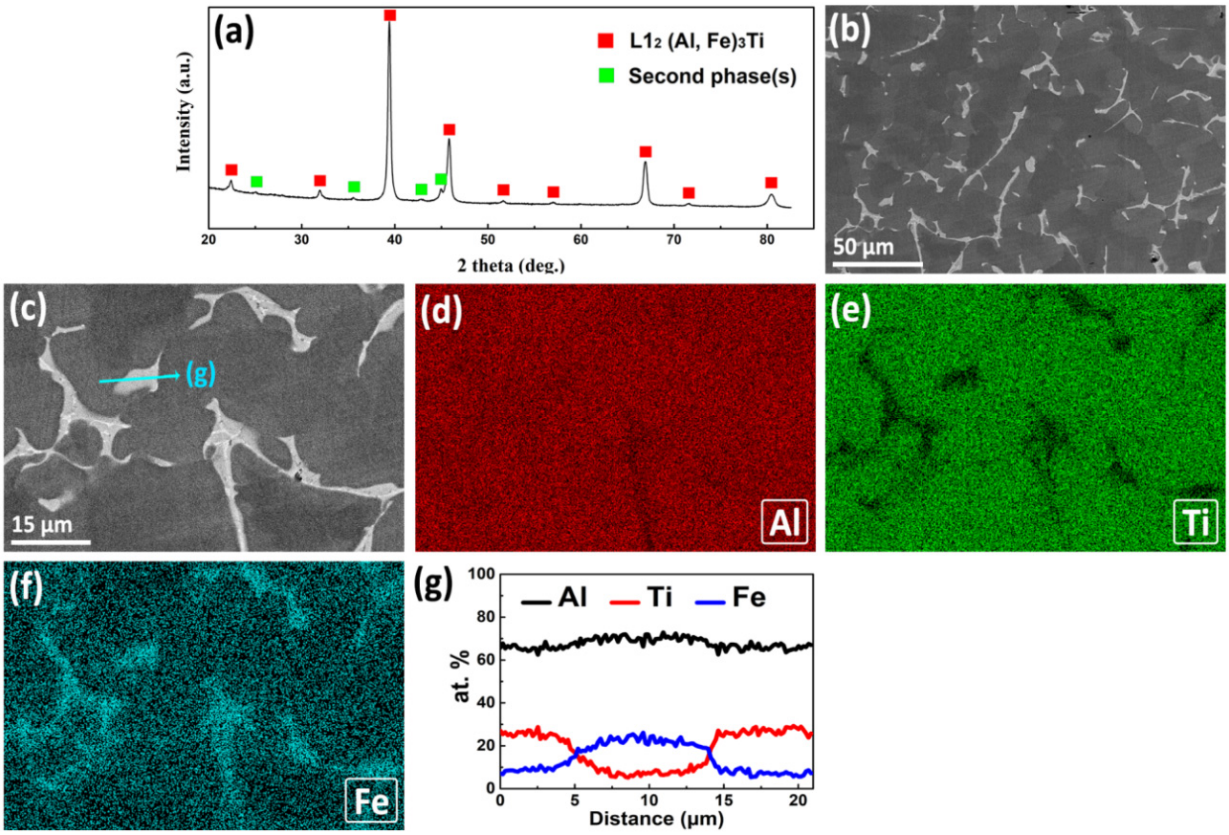


Figure 4. Microstructure characterization for S-$Al_{67}Ti_{25}Fe_8$. (**a**) XRD pattern; (**b**,**c**) SEM-BSE images; (**d**–**f**) elemental distributions of the same area shown in (**c**); (**g**) elemental distribution along the blue line shown in (**c**).

In binary Al_3Ti, the $D0_{22}$ structure is more stable, in which the charge transfers from Al to Ti, contributing to strong bonding strength. When the third element, which is less electropositive than Al, is added, it substitutes for Al and takes electrons from Al and consequently suppresses the charge transfer from Al to Ti. As a result, the $L1_2$ structure $(Al,M)_3Ti$ becomes more stable than $D0_{22}$ $(Al,M)_3Ti$, i.e., the $L1_2$ structure is stabilized by adding third elements. More discussions with more details and references have been given in Section 4. The phase transformation from $D0_{22}$ to $L1_2$ certainly affects the mechanical properties, i.e., the ductility increases at the expense of hardness. The corresponding change in the balance between the hardness and ductility consequently influences the combination of hardness and toughness and, thus, the wear resistance. The resultant variations in wear resistance caused by the phase transformation are reported in the next section.

Figure 5 illustrates the microstructure of the 30 wt.% SiC particle-reinforced Al-matrix composite (denoted as S-Al/SiC_p), which was used as a reference material when evaluating the wear resistance of the $D0_{22}$ Al_3Ti-predominant S-Al_3Ti alloy and the $L1_2$ $(Al, Fe)_3Ti$-predominant S-$Al_{67}Ti_{25}Fe_8$ alloy. As the SEM-BSE image in Figure 5a shows, dense particles in dark were distributed in the light gray matrix. According to the corresponding EDS maps shown in Figure 5b–d, the dark particles were SiC and the light gray matrix was Al. The SiC particles significantly hardened the Al matrix, playing an important role in contributing to the wear resistance of the S-Al/SiC_p composite.

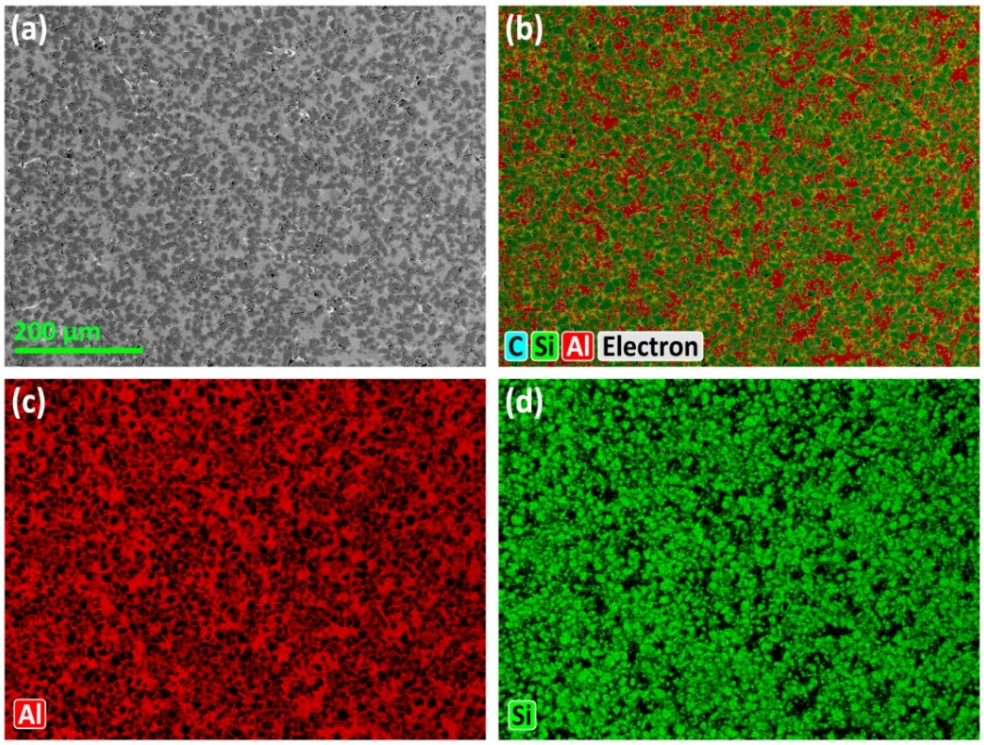


Figure 5. Microstructure of S-Al/SiC_p composite. (**a**) SEM-BSE image in secondary electron mode. (**b**–**d**) Elemental distribution of the same area shown in (**a**).

3.2. Wear Behavior

The Rockwell hardness values of three samples, S-Al_3Ti, S-$Al_{67}Ti_{25}Fe_8$, and S-Al/SiC_p as a reference material, were measured at room temperature using a conical diamond indenter under a load of 60 kgf. Results of the tests are displayed in Figure 6. As shown, S-Al_3Ti exhibited the highest hardness amongst the three samples. S-$Al_{67}Ti_{25}Fe_8$ showed a slightly lower hardness, compared to that of S-Al_3Ti, suggesting that the transformation of the $D0_{22}$ phase predominant in S-Al_3Ti to $L1_2$ $(Al, Fe)_3Ti$ in S-$Al_{67}Ti_{25}Fe_8$ did not decrease the hardness much. Although having densely distributed reinforcing SiC particles, the hardness of the S-Al/SiC_p composite was markedly lower than those of the two alloys.

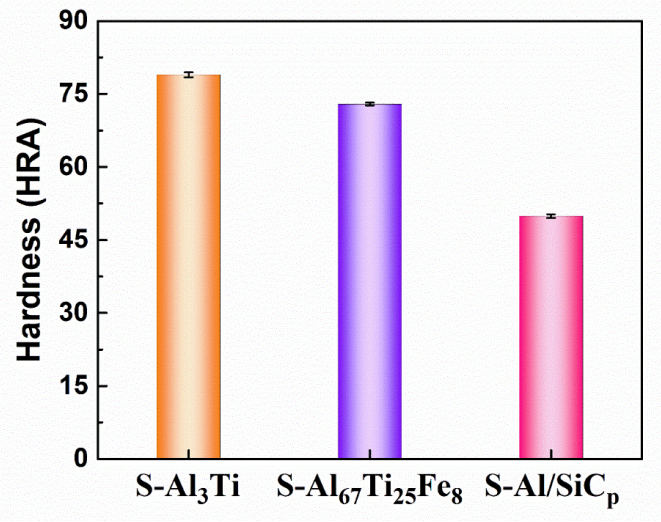


Figure 6. Rockwell hardness using a conical diamond indenter under load of 60 kgf.

In this study, S-Al/SiC_p was used as a reference material for the comparison purpose. S-Al_3Ti and S-$Al_{67}Ti_{25}Fe_8$ had relatively low densities (~3.17 and 3.48 g/cm^3, respectively). The present study was conducted with the motivation to develop Al_3Ti-based lightweight alloys for tribological applications. Since the commercial S-Al/SiC_p possessed a good wear resistance with its density around 2.84 g/cm^3, close to those of the above-mentioned alloys, selecting this well-known material as a reference material should facilitate this comparison with relatively quantitative information.

Indents caused by a diamond indenter with a square pyramid shape under a load of 15 kgf were observed under SEM in the second electron (SE) mode. The obtained images are displayed in Figure 7, showing that S-Al_3Ti (Figure 7a) is the hardest, S-$Al_{67}Ti_{25}Fe_8$ (Figure 7b) is less hard, and Al/SiC_p (Figure 7c) is the softest among the three materials. Comparing the morphologies of the indents on S-Al_3Ti and S-$Al_{67}Ti_{25}Fe_8$, the zone around the indent on the former showed some wrinkles and micro-cracks, while the latter had much less these features, indicating that S-Al_3Ti is brittle or less ductile, compared to S-$Al_{67}Ti_{25}Fe_8$.

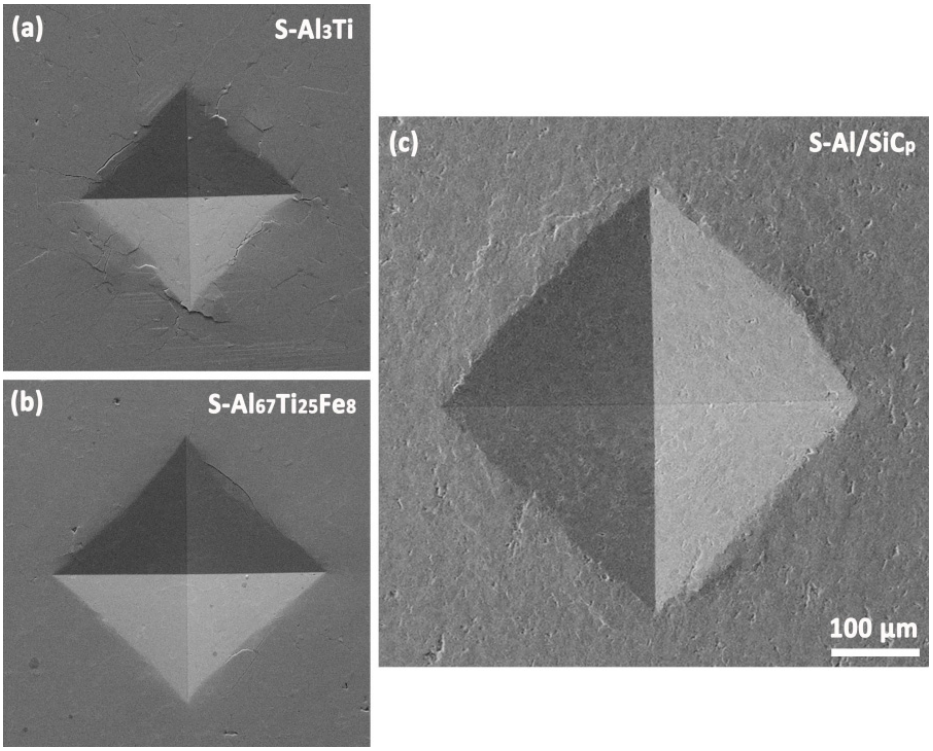


Figure 7. Indents caused by a diamond indenter with square pyramid shape under load of 15 kgf: (**a**) S-Al_3Ti. (**b**) S-$Al_{67}Ti_{25}Fe_8$. (**c**) S-Al/SiC_p.

The volume losses of the samples after sliding wear testing under 3 N in the ambient environment for 30 min are shown in Figure 8a, and the wear track profiles are displayed in Figure 8b_1–d_2. In spite of the lower hardness, the alloy S-$Al_{67}Ti_{25}Fe_8$ demonstrated a higher wear resistance than the harder alloy S-Al_3Ti, which should benefit from its $L1_2$ (Al, $Fe)_3Ti$ phase with higher plasticity than that of the harder but less ductile $D0_{22}$ Al_3Ti phase in S-Al_3Ti. A combination of strength and ductility/plasticity can make a reasonably hard material tougher against wear attacks. The composite S-Al/SiC_p showed the lowest wear resistance due to its lowest hardness among the three materials.

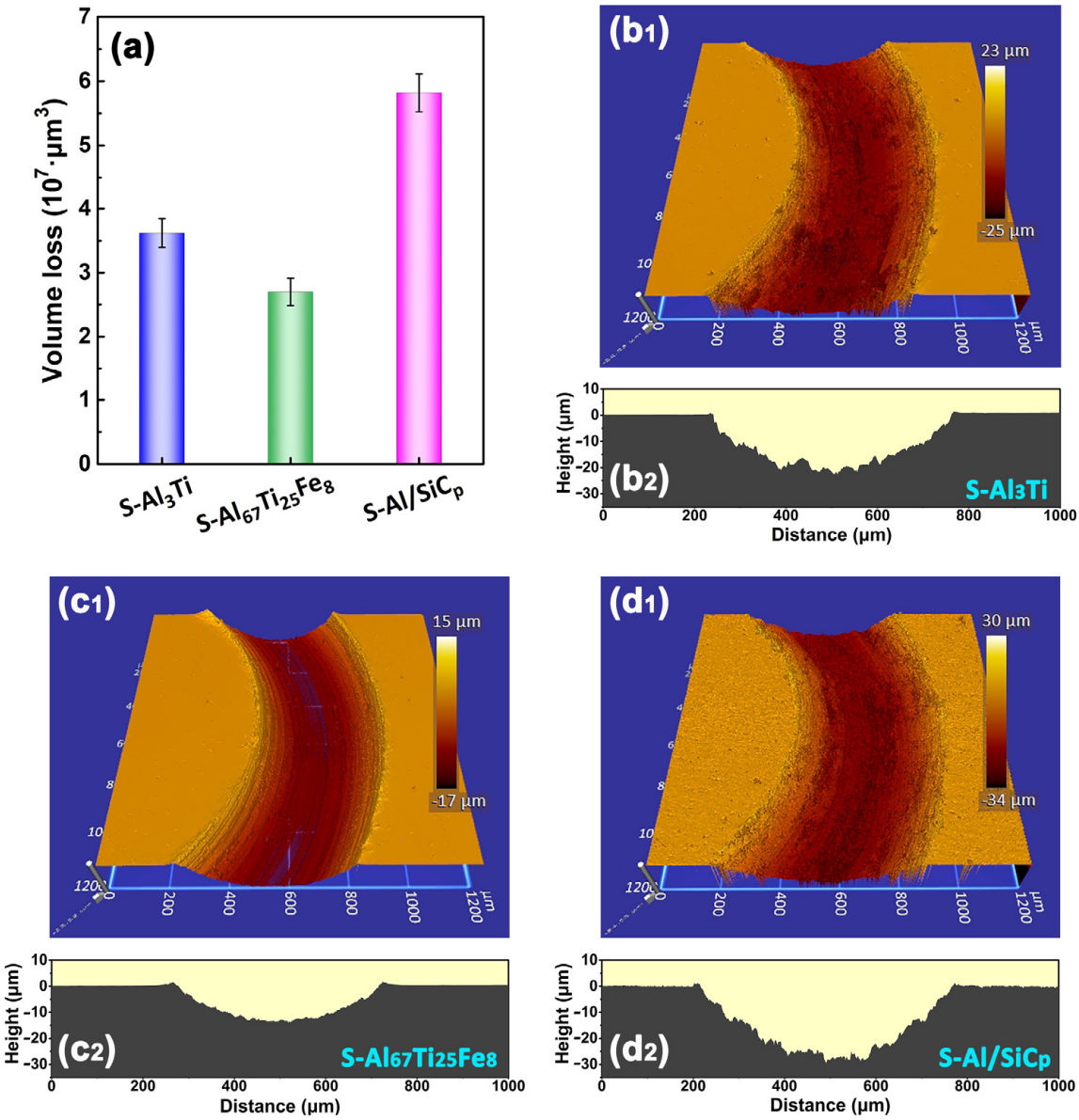


Figure 8. Volume losses caused by wear under 3 N for 20 min at ambient. (**a**) Volume losses; 3D and cross-sectional wear track profiles of (**b1**,**b2**) S-Al_3Ti, (**c1**,**c2**) S-$Al_{67}Ti_{25}Fe_8$, and (**d1**,**d2**) S-Al/SiC_p.

In order to elucidate the wear mechanisms for different performances of the three materials during wear tests, their worn surface morphologies were observed and analyzed, as illustrated in Figures 9 and 10. S-Al_3Ti showed its worn surface involving wear and oxidation caused by frictional heating [38,39], as evidenced by the detected oxygen distribution shown in the inset of Figure 9a_1, and the oxide scale spallation shown in Figure 9a_2,a_3 (yellow arrow). In addition, surface fragmentation was also observed on S-Al_3Ti near the area where a piece of oxide scale was removed, as shown in Figure 9a_2 (magenta arrow), due to its lower plasticity or brittleness, compared to that of S-$Al_{67}Ti_{25}Fe_8$. In contrast, the worn surface of S-$Al_{67}Ti_{25}Fe_8$ showed more abrasive wear characteristics with scratching grooves as illustrated in Figure 9b_1. Oxidation occurred on the surface as well, but it appeared to be much less, as one may see in the oxygen distribution shown in the inset of Figure 9b_1. Very tiny craters were observed on or around the Fe-rich second phase (marked by yellow circles) connecting to the dominant $L1_2$ (Al, Fe)$_3$Ti phase, as shown in Figure 9b_2, which could be an indication of the brittleness of the Fe-rich Ti-depleted second phases in comparison with that of the $L1_2$ phase. Due to the mechanical difference between the

second phase and the $L1_2$ phase, the local stress concentrations induced by incompatible deformations of the two phases under the wearing stress could induce local beak-off, which could trigger crack initiation. During the continuous wear process, micro-cracks could propagate and lead to eventual wear volume loss.

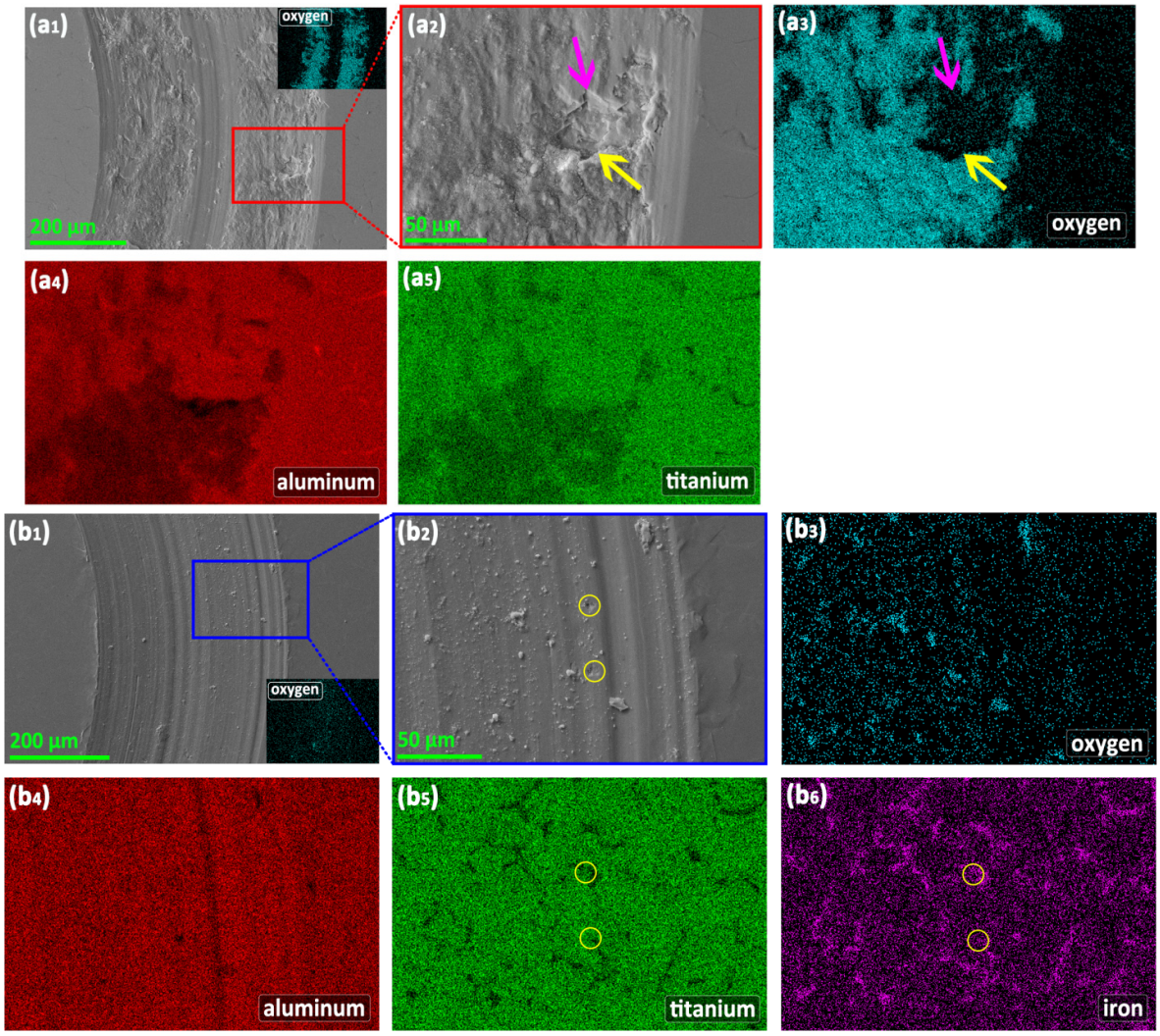


Figure 9. SEM-SE images and EDS mapping analysis of the worn surfaces of (**a$_1$**–**a$_5$**) S-Al_3Ti and (**b$_1$**–**b$_6$**) S-$Al_{67}Ti_{25}Fe_8$. (**a$_1$**,**a$_2$**) SEM-SE images of worn surface morphology; (**a$_3$**–**a$_5$**) O, Al, and Ti distribution of the same area in (**a$_2$**). (**b$_1$**,**b$_2$**) SEM-SE images of worn surface morphology; (**b$_3$**–**b$_6$**) O, Al, Ti, and Fe distribution of the same area in (**b$_2$**). The insets in (**a$_1$**,**b$_1$**) are the oxygen distribution of the surface area in (**a$_1$**,**b$_1$**), respectively.

With higher hardness, S-Al_3Ti was supposed to be subject to less abrasive wear damage when compared to S-$Al_{67}Ti_{25}Fe_8$. However, the wear damage to S-Al_3Ti is severer than that to S-$Al_{67}Ti_{25}Fe_8$, as demonstrated by Figure 9a$_1$,b$_1$. This happened, as discussed earlier. The less protective oxide scale on S-Al_3Ti with obvious spallation and surface fragmentation could make the alloy less resistant to wear attack. The oxide spall-off along with abraded material pieces of material may act as debris to result in additional wear damage [40,41]. Thus, the brittleness of the substrate, oxidation, and the spallation of the oxide scales could be responsible for the larger wear volume loss of S-Al_3Ti, compared to that of S-$Al_{67}Ti_{25}Fe_8$.

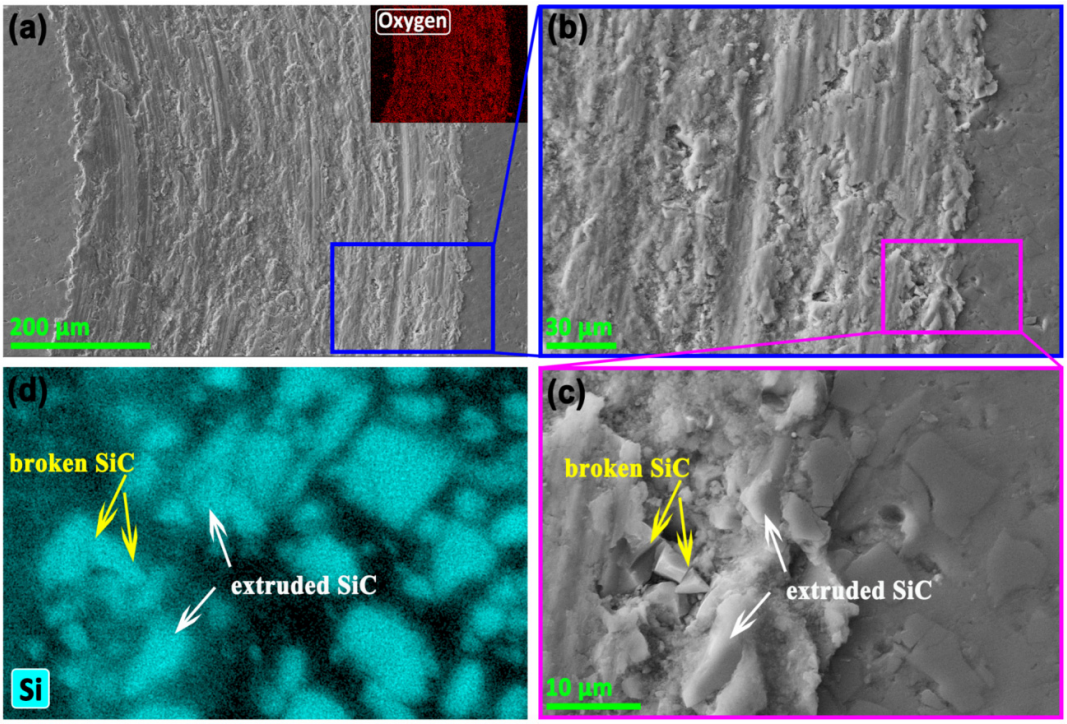


Figure 10. SEM-SE images and EDS mapping of the worn surface of the S-Al/SiC_p composite. (**a**–**c**) Worn surface morphology with different magnifications; (**d**) silicon distribution of the same area in (**c**). The inset in (**a**) shows the oxygen distribution on the worn surface area marked by a blue rectangular frame.

Regarding the wear of S-$Al_{67}Ti_{25}Fe_8$ with decreased hardness and increased toughness, less oxidation was involved, evidenced by less oxygen contents inside and outside the wear track (see the inserted figure in Figure 9b_1), and no oxide scale spallation was observed (see Figure 9b_1,b_2). The reduced brittleness with maintained reasonable hardness led to reduced abrasive wear. Consequently, S-$Al_{67}Ti_{25}Fe_8$ showed a lower volume loss or higher wear resistance, compared to S-Al_3Ti. Regarding oxidation, as shown in Figure 9b_3, oxygen was still detected, but oxidation was markedly less, which can be ascribed to two possible reasons: (1) the oxide film was compacted and protective, so the oxide growth was slow, leading to the formation of a thin oxide film; and (2) the thin oxide film was removed during the wear testing, and re-growth was slow due to higher protectiveness of the oxide film. Bear in mind that a protective oxide film can form rapidly in the initial stage and the following growth becomes slow since the protective film more effectively hinders the diffusion of metallic atoms and oxygen, the continuous oxidation can thus be stopped. A protective oxide film helps reduce wear and minimize synergistic attacks by wear and oxidation. However, it is not very clear why the Fe addition improved the oxidation behavior or the protectiveness of the oxide scale on S-$Al_{67}Ti_{25}Fe_8$. Analyzing the influences of Fe on the stability or cohesive energy, the adherence and mechanical properties of the oxide scale on the S-$Al_{67}Ti_{25}Fe_8$ substrate would help understand the role that the Fe addition plays. These will be included in our follow-up studies.

It should also be mentioned that no sign of adhesive wear was noticed. In the obtained EDS maps, Si was not observed due to its insufficient content, implying that the adhesive transfer from the Si_3N_4 ball to the sample under study was negligible. There were also no noticeable patches of material peel-off on the alloy samples, i.e., alloy transfer. Thus, adhesive wear should have little contribution to wear in the present case, and abrasive wear was the dominant wear mechanism with influences of synergistical oxidation for both S-Al_3Ti and S-$Al_{67}Ti_{25}Fe_8$ at different extents.

The worn surface of S-Al/SiC_p, as a reference material, which exhibited the lowest wear resistance among the three samples due to its lower hardness, is illustrated in Figure 10. The characteristics of abrasive wear with obvious plastic deformation were observed as shown in Figure 10a. The enlarged image in Figure 10b reveals dense wear debris, abrasive grooves, and some adhesive patches. During the wear test, the soft Al matrix experienced severe plastic deformation under the wearing force, forming flakes that adhered to the surface during repeated sliding when oxidation was also involved, as evidenced by the oxygen distribution shown in the inset of Figure 10a. In S-Al/SiC_p, the Al matrix may not be strong enough to effectively maintain the reinforcing SiC particles during the wear process. Thus, SiC particles may be either detached from the Al matrix or extruded along with the plastically deformed Al matrix, as illustrated in Figure 10c,d, thereby failing to effectively protect the surface from wear attack. As a result, S-Al/SiC_p showed considerably larger volume loss and lower wear resistance than both S-Al_3Ti and S-$Al_{67}Ti_{25}Fe_8$.

4. Discussion

The $D0_{22}$ structure is proven to be the most stable structure of stoichiometric Al_3Ti alloy, while the $L1_2$ structure is a metastable structure which may be obtained under non-equilibrium processing condition, such as rapid solidification [42,43] and mechanical alloying [44,45]. The metastable $L1_2$ structure prepared by mechanical alloying may transform (through $D0_{23}$ structure) to stable $D0_{22}$ structure by heating processes [44,46]. First-principals calculations suggest that, in the $D0_{22}$ structure, Ti atoms gain charges and Al atoms lose charges, while in $L1_2$ structure, the situation is opposite [12]. As indicated earlier, adding an appropriate amount of less electropositive third elements such as Fe and Cr can replace Al, take electrons from Al, and consequently suppress the charge transfer from Al to Ti, thus stabilizing the cubic $L1_2$ structure and leading to the transformation of the $D0_{22}$ structure to the $L1_2$ one [22,23]. The resultant $L1_2$ structure keeps stable in an as-cast and homogenized state [16], indicating that adding proper third elements is an effective approach to obtain a stable $L1_2$ structure near stoichiometric Al_3Ti composition, leading to improved plasticity. The above points have also been confirmed by the present study on the modification of Al_3Ti with Fe addition for enhanced wear resistance.

For dry sliding wear of materials in the ambient environment, mechanical properties, such as strength and ductility that, along with hardness, determine the toughness of a material, are considered to be the most important factors which govern the wear resistance. The $D0_{22}$-to-$L1_2$ transformation from S-Al_3Ti to S-$Al_{67}Ti_{25}Fe_8$ improved the ductility (revealed by indentation marks in Figure 7) without losing much hardness (see Figure 6), leading to enhanced wear resistance, as shown in Figure 8. In addition to Fe, other elements such as Cr, Mn, Ni, Cu, and Ag can also stabilize $L1_2$ $(Al, M)_3Ti$ due to the difference in electronegativity between the constituent atoms, and the energy difference between the $D0_{22}$ and $L1_2$ structures [22,47]. Although little research on the wear behavior of $D0_{22}$ Al_3Ti and $L1_2$ $(Al, M)_3Ti$ is reported, the beneficial effects of these elements on the wear resistance of Al_3Ti can be expected based on the present study on the role of Fe addition in improving the wear resistance of the Al_3Ti alloy.

In this work, both S-Al_3Ti and S-$Al_{67}Ti_{25}Fe_8$ were subject to surface abrasion and oxidation to different extents. Although S-Al_3Ti is harder than S-$Al_{67}Ti_{25}Fe_8$, it showed lower wear resistance than the latter, ascribed to the fact that its higher brittleness and formation of a less protective oxide scale resulted in more wear damage, as described earlier [48,49]. It should also be mentioned that a brittle substrate may deteriorate the adherence of its oxide scale due to lowered flexibility that may elevate the interfacial stress if the chemical interaction and lattice mismatch between the oxide scale and substrate remain the same or similar, thus accelerating the oxide scale spallation and promoting the wear-oxidation synergy, leading to more wear for the brittle or less tough S-Al_3Ti, compared to that of the more plastic S-$Al_{67}Ti_{25}Fe_8$. In addition, the oxide scale spall-off mixed with wear debris could result in extra wear damage [41].

5. Conclusions

In this work, two Al_3Ti-based alloys, S-Al_3Ti containing ~97 vol.% of $D0_{22}$ Al_3Ti phase, and S-$Al_{67}Ti_{25}Fe_8$ containing ~93 vol.% of $L1_2$ $(Al, Fe)_3Ti$ phase, were fabricated using an arc melting process, with the main objective being to investigate how the wear resistance of Al_3Ti was influenced by the transformation from the $D0_{22}$ to the $L1_2$ structure caused by alloying with a third element, Fe. Their wear resistances were evaluated and compared with a commercial Al-matrix composite reinforced by 30 wt.% SiC particles (S-Al/SiC_p) as a reference material. The following conclusions were drawn:

(a) Alloying Al_3Ti with Fe, which may partially substitute Al, successfully transformed the $D0_{22}$ Al_3Ti to $L1_2$ $(Al, Fe)_3Ti$, leading to improved ductility or toughness at the expense of hardness;
(b) S-Al_3Ti experienced oxide scale spallation and surface fragmentation due to its brittleness, resulting in higher wear volume loss;
(c) S-$Al_{67}Ti_{25}Fe_8$ exhibited lowered abrasive wear due to a reasonable combination of hardness and ductility/toughness, thus increasing its wear resistance;
(d) Both the S-Al_3Ti and S-$Al_{67}Ti_{25}Fe_8$ alloys exhibited higher wear resistances than the commercial S-Al/SiC_p composite. The $(Al, M)_3Ti$ alloy series can be further optimized and is promising as lightweight materials for tribological applications.

The reported in this article is a preliminary study showing the potential anti-wear or tribological applications of lightweight Al_3Ti-based $L1_2$-structure material fabricated by arc melting. In the follow-up work, efforts will be made to further improve or optimize the base alloy by adding several third alloying elements with appropriate compositions to improve the toughness. In addition, potential combinations of $L1_2$-structure Al_3Ti-based lightweight material with other materials such as carbides as the reinforcing phases should be explored to develop composites with a superior strength–toughness combination for tribological applications under specific or extreme conditions.

Author Contributions: Conceptualization, G.D. and D.L.; methodology, J.Y., A.H., A.K., R.F., A.V., W.C. and D.L.; validation, J.Y., A.H., D.Z., A.K., R.F., A.V., W.C. and D.L.; formal analysis, G.D.; investigation, G.D. and D.Z.; resources, R.F., A.V., W.C. and D.L.; data curation, A.H. and D.Z.; writing—original draft, G.D.; writing—review and editing, R.F., A.V., W.C. and D.L.; supervision, D.L.; project administration, D.L.; funding acquisition, W.C. and D.L. All authors have read and agreed to the published version of the manuscript.

Funding: This research was funded by the Natural Science and Engineering Research Council of Canada (NSERC AMA ALLRP 567506-21 Li), NSERC-NRCan (ALLRP 586454-23), Trimay and Mitacs (MI MA IT29134 Kumar/Xu/Li), and the Academician Workstation in Yunnan Province (Grant No. 202305AF150019).

Data Availability Statement: The original contributions presented in the study are included in the article, further inquiries can be directed to the corresponding author.

Conflicts of Interest: The authors declare no conflict of interest.

References

1. He, Z.Y.; Wang, Z.X.; Liu, X.P.; Han, P.D. Preparation of TiAl–Cr surface alloy by plasma-surface alloying technique. *Vacuum* **2013**, *89*, 280–284. [CrossRef]
2. Uenishi, K.; Kobayashi, K.F. Processing of intermetallic compounds for structural applications at high temperature. *Intermetallics* **1996**, *4*, S95–S101. [CrossRef]
3. Wei, N.; Han, X.; Zhang, X.; Cao, Y.; Guo, C.; Lu, Z.; Jiang, F. Characterization and properties of intermetallic Al_3Ti alloy synthesized by reactive foil sintering in vacuum. *J. Mater. Res.* **2016**, *31*, 2706–2713. [CrossRef]
4. Russell, A.M. Ductility in Intermetallic Compounds. *Adv. Eng. Mater.* **2003**, *5*, 629–639. [CrossRef]
5. Bochenek, K.; Basista, M. Advances in processing of NiAl intermetallic alloys and composites for high temperature aerospace applications. *Prog. Aerosp. Sci.* **2015**, *79*, 136–146. [CrossRef]
6. Li, Z.; Gao, W. High temperature corrosion of intermetallics. In *Intermetallics Research Progress*; Nova Science Publisher: Hauppauge, NY, USA, 2008; pp. 1–64.

7. Nayak, S.S.; Murty, B.S. Synthesis and stability of $L1_2$–Al_3Ti by mechanical alloying. *Mater. Sci. Eng. A* **2004**, *367*, 218–224. [CrossRef]
8. Schoenitz, M.; Zhu, X.; Dreizin, E.L. Mechanical alloys in the Al-rich part of the Al-Ti binary system. *J. Metastable Nanocryst. Mater.* **2004**, *20*, 455–461. [CrossRef]
9. Yamaguchi, M.; Umakoshi, Y.; Yamane, T. Plastic deformation of the intermetallic compound Al_3Ti. *Philos. Mag. A* **1987**, *55*, 301–315. [CrossRef]
10. Huang, Y.; Jiang, J. A Critical Review of von Mises Criterion for Compatible Deformation of Polycrystalline Materials. *Crystals* **2023**, *13*, 244. [CrossRef]
11. Schwarz, R.B.; Desch, P.B.; Srinivasan, S. Phase Stability of Al_3X Alloys (X = Ti, Zr, Hf). In *Statics and Dynamics of Alloy Phase Transformations*; Turchi, P.E.A., Gonis, A., Eds.; Springer: Boston, MA, USA, 1994; pp. 81–101.
12. Hussain, A.; Mehmood, S.; Rasool, N.; Li, N.; Dharmawardhana, C.C. Electronic structure, mechanical and optical properties of $TiAl_3$ ($L1_2$ & $D0_{22}$) via first-principles calculations. *Chin. J. Phys.* **2016**, *54*, 319–328. [CrossRef]
13. Nakayama, Y.; Mabuchi, H. Formation of ternary $L1_2$ compounds in Al_3Ti-base alloys. *Intermetallics* **1993**, *1*, 41–48. [CrossRef]
14. Mabuchi, H.; Kito, A.; Nakamoto, M.; Tsuda, H.; Nakayama, Y. Effects of manganese on the $L1_2$ compound formation in Al_3Ti-based alloys. *Intermetallics* **1996**, *4*, S193–S199. [CrossRef]
15. Gengxiang, H.; Shipu, C.; Xiaohua, W.; Xiaofu, C. Plastic deformation and fracture behavior of a Fe-modified Al_3Ti-base $L1_2$ intermetallic alloy. *J. Mater. Res.* **2011**, *6*, 957–963. [CrossRef]
16. Mabuchi, H.; Tsuda, H.; Matsui, T.; Morii, K. Microstructure and mechanical properties of ternary $L1_2$ intermetallic compound in Al–Ti–Cr system. *Mater. Trans. JIM* **1997**, *38*, 560–565. [CrossRef]
17. Prakash, U.; Buckley, R.A.; Jones, H.; Sellars, C.M. DO_{22} to $L1_2$ transition in intermetallic systems. *J. Mater. Sci.* **1992**, *27*, 2001–2004. [CrossRef]
18. Varin, R.A.; Zbroniec, L.; Chiu, C. Observations of crack tip process zones in cubic titanium trialuminide intermetallics. *Intermetallics* **2001**, *9*, 937–941. [CrossRef]
19. Tian, W.H.; Nemoto, M. Phase decomposition and hardening of Ag-modified $L1_2$ Al_3Ti. *Intermetallics* **1998**, *6*, 193–200. [CrossRef]
20. Heilmaier, M.; Handtrack, D.; Varin, R.A. Creep properties of boron-doped dual-phase Ti-rich $L1_2$-based trialuminide intermetallics. *Scr. Mater.* **2003**, *48*, 1409–1414. [CrossRef]
21. Varin, R.A.; Zbroniec, L.; Wang, Z.G. Fracture toughness and yield strength of boron-doped, high (Ti+Mn) $L1_2$ titanium trialuminides. *Intermetallics* **2001**, *9*, 195–207. [CrossRef]
22. George, E.P.; Pope, D.P.; Fu, C.L.; Schneibel, J.H. Deformation and Fracture of $L1_2$ Trialuminides. *ISIJ Int.* **1991**, *31*, 1063–1075. [CrossRef]
23. Ghosh, G.; van de Walle, A.; Asta, M. First-Principles Phase Stability Calculations of Pseudobinary Alloys of $(Al,Zn)_3Ti$ with $L1_2$, $D0_{22}$, and $D0_{23}$ Structures. *J. Phase Equilibria Diffus.* **2007**, *28*, 9–22. [CrossRef]
24. Xu, X.; Xu, W.; Ederveen, F.H.; van der Zwaag, S. Design of low hardness abrasion resistant steels. *Wear* **2013**, *301*, 89–93. [CrossRef]
25. Boulechfar, R.; Sayad, D.; Khenioui, Y.; Meradji, H.; Ghemid, S.; Khenata, R.; Bin-Omran, S.; Bouhemadou, A.; Goumri-Said, S. Theoretical investigations of Zr-concentration influence on the thermodynamic, elastic, electronic, and structural stability of $D0_{22}/L1_2$-Al_3Ti. *Eur. Phys. J. B* **2024**, *97*, 1. [CrossRef]
26. Milman, Y.V.; Miracle, D.B.; Chugunova, S.I.; Voskoboinik, I.V.; Korzhova, N.P.; Legkaya, T.N.; Podrezov, Y.N. Mechanical behaviour of Al_3Ti intermetallic and L12 phases on its basis. *Intermetallics* **2001**, *9*, 839–845. [CrossRef]
27. Luo, J.; Liu, M.; Ma, L. Origin of friction and the new frictionless technology—Superlubricity: Advancements and future outlook. *Nano Energy* **2021**, *86*, 106092. [CrossRef]
28. Xu, Z.; Li, D.Y.; Chen, D.L. Effect of Ti on the wear behavior of AlCoCrFeNi high-entropy alloy during unidirectional and bi-directional sliding wear processes. *Wear* **2021**, *476*, 203650. [CrossRef]
29. Akonko, S.; Li, D.Y.; Ziomek-Moroz, M. Effects of cathodic protection on corrosive wear of 304 stainless steel. *Tribol. Lett.* **2005**, *18*, 405–410. [CrossRef]
30. Yin, S.; Li, D.Y. Effects of prior cold work on corrosion and corrosive wear of copper in HNO_3 and NaCl solutions. *Mater. Sci. Eng. A* **2005**, *394*, 266–276. [CrossRef]
31. Faghihi, S.; Li, D.; Szpunar, J.A. Tribocorrosion behaviour of nanostructured titanium substrates processed by high-pressuretorsion. *Nanotechnology* **2010**, *21*, 485703. [CrossRef]
32. Hutchings, I.; Shipway, P. *Tribology: Friction and Wear of Engineering Materials*; Butterworth-Heinemann: Oxford, UK, 2017.
33. He, H.-B.; Han, W.-Q.; Li, H.-Y.; Li, D.-Y.; Yang, J.; Gu, T.; Deng, T. Effect of deep cryogenic treatment on machinability and wear mechanism of TiAlN coated tools during dry turning. *Int. J. Precis. Eng. Manuf.* **2014**, *15*, 655–660. [CrossRef]
34. Budinski, K.G.; Budinski, S.T. *Tribomaterials: Properties and Selection for Friction, Wear, and Erosion Applications*; ASM International: Almere, The Netherlands, 2021.
35. Tong, X.; Zhang, H.; Li, D.Y. Effect of annealing treatment on mechanical properties of nanocrystalline α-iron: An atomistic study. *Sci. Rep.* **2015**, *5*, 8459. [CrossRef] [PubMed]
36. Li, D.Y.; Szpunar, J.A. A possible role for surface packing density in the formation of {111} texture in solidified FCC metals. *J. Mater. Sci. Lett.* **1994**, *13*, 1521–1523. [CrossRef]
37. Bunge, H.J. *Texture Analysis in Materials Science: Mathematical Methods*; Elsevier: Amsterdam, The Netherlands, 2013.

38. Knothe, K.; Liebelt, S. Determination of temperatures for sliding contact with applications for wheel-rail systems. *Wear* **1995**, *189*, 91–99. [CrossRef]
39. Quinn, T.F.J. Oxidational wear modelling: I. *Wear* **1992**, *153*, 179–200. [CrossRef]
40. Garza-Montes-de-Oca, N.F.; Rainforth, W.M. Wear mechanisms experienced by a work roll grade high speed steel under different environmental conditions. *Wear* **2009**, *267*, 441–448. [CrossRef]
41. Cheng, X.; Jiang, Z.; Wei, D.; Wu, H.; Jiang, L. Adhesion, friction and wear analysis of a chromium oxide scale on a ferritic stainless steel. *Wear* **2019**, *426–427*, 1212–1221. [CrossRef]
42. Majumdar, A.; Muddle, B.C. Microstructure in rapidly solidified Al-Ti alloys. *Mater. Sci. Eng. A* **1993**, *169*, 135–147. [CrossRef]
43. Guo, J.Q.; Ohtera, K.; Kita, K.; Shibata, T.; Inoue, A.; Masumoto, T. New metastable phases in rapidly solidified Al-Zr and Al-Ti alloys with high solute contents. *Mater. Sci. Eng. A* **1994**, *181–182*, 1397–1404. [CrossRef]
44. Srinivasan, S.; Desch, P.B.; Schwarz, R.B. Metastable phases in the Al_3X (X = Ti, Zr, and Hf) intermetallic system. *Scr. Metall. Mater.* **1991**, *25*, 2513–2516. [CrossRef]
45. Klassen, T.; Oehring, M.; Bormann, R. Microscopic mechanisms of metastable phase formation during ball milling of intermetallic TiAl phases. *Acta Mater.* **1997**, *45*, 3935–3948. [CrossRef]
46. Colinet, C.; Pasturel, A. Ab initio calculation of the formation energies of $L1_2$, $D0_{22}$, $D0_{23}$ and one dimensional long period structures in $TiAl_3$ compound. *Intermetallics* **2002**, *10*, 751–764. [CrossRef]
47. Carlsson, A.E.; Meschter, P.J. Relative stability of LI_2, DO_{22}, and DO_{23} structures in MAl_3 compounds. *J. Mater. Res.* **1989**, *4*, 1060–1063. [CrossRef]
48. Qiu, X.W.; Zhang, Y.P.; Liu, C.G. Effect of Ti content on structure and properties of $Al_2CrFeNiCoCuTi_x$ high-entropy alloy coatings. *J. Alloys Compd.* **2014**, *585*, 282–286. [CrossRef]
49. Li, Y.; Liang, H.; Nie, Q.; Qi, Z.; Deng, D.; Jiang, H.; Cao, Z. Microstructures and Wear Resistance of $CoCrFeNi_2V_{0.5}Ti_x$ High-Entropy Alloy Coatings Prepared by Laser Cladding. *Crystals* **2020**, *10*, 352. [CrossRef]

Disclaimer/Publisher's Note: The statements, opinions and data contained in all publications are solely those of the individual author(s) and contributor(s) and not of MDPI and/or the editor(s). MDPI and/or the editor(s) disclaim responsibility for any injury to people or property resulting from any ideas, methods, instructions or products referred to in the content.